Supplementary Material

Chip-scale metalens microscope for wide-field and depth-of-field imaging

Xin Ye[a,b], Xiao Qian[a,b], Yuxin Chen[a,b], Rui Yuan[a], Xingjian Xiao[a,b], Chen Chen[a,b], Wei Hu[a], Chunyu Huang[a], Shining Zhu[a,b], and Tao Li [a,b,*]

[a]Nanjing University, National Laboratory of Solid State Microstructures, Key Laboratory of Intelligent Optical Sensing and Integration, Jiangsu Key Laboratory of Artificial Functional Materials, College of Engineering and Applied Sciences, Nanjing, China, 210093

[b]Collaborative Innovation Center of Advanced Microstructures, Nanjing, China, 210093

Section 1: Materials and methods.

Refractive Index Measurement. A 1-μm-thick silicon nitride film was deposited on the fused silica substrate by plasma-enhanced chemical vapor deposition (PECVD). Then, the wavelength dependent (400-800 nm) refractive index was measured by using the spectroscopic ellipsometer.

Sample Fabrication. A 1-μm-thick silicon nitride film was deposited on a 200-μm-thick/500-μm-thick fused silica substrate by PECVD at 300 °C. Positive electron beam resist (200 nm, PMMA A4) was then spin-coated. The metalens pattern was written in the resist using electron beam lithography (EBL, ELS-F125, Elionix). After developing the resist, the pattern was transferred into a 40-nm-thick chromium layer deposited by electron beam evaporation (EBE) using the lift-off technique. The pattern chromium served as hard mask for the dry etching of the 1-μm-thick SiN_x layer in a mixture of CHF3 and SF6 plasma (Oxford Instruments, PlasmaPro100 Cobra300). Finally, the chromium mask was removed using a solution of ammonium cerium nitrate.

Optical measurements. A white LED (Daheng Optics GCI-060411) with band-pass filters at bandwidth of 10 nm (Thorlabs, FB-10 series) is employed as the illumination source. The adjustable circular polarized filter (thickness = 220 μm) are used to select the incident circular polarization state. The PMID is mounted on an assembled translation stage to adjustable along the optical direction. More detailed can be found in the Fig. S2.

Section 2: Design and fabrication of single metalens.

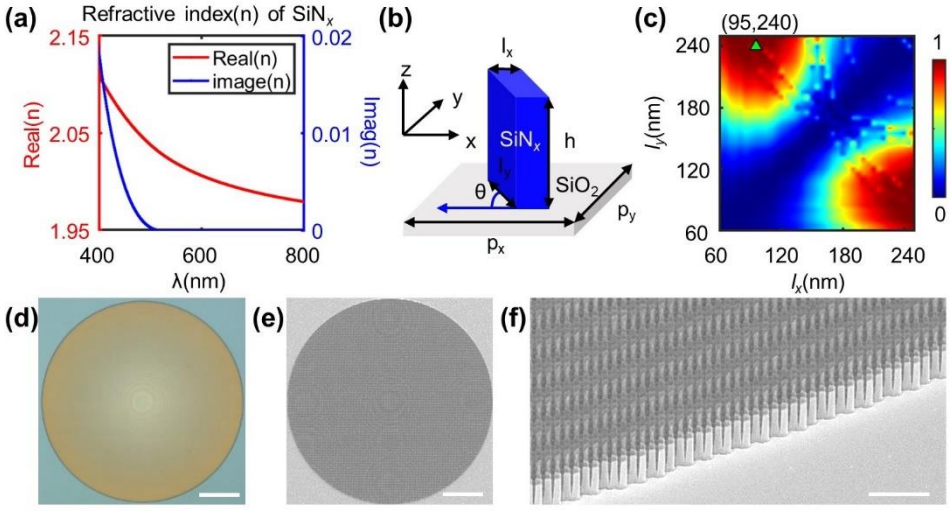

Fig. S1 Design and fabrication of single metalens. (a) The real and imaginary part of the refractive index (n) of 173.4 nm thick silicon nitride film is measured using spectroscopic ellipsometry. (b) Perspective view of the metasurface unit-cell formed by SiN_x nanofin deposited on a silica substrate. (c) Simulated polarization conversion rate of each nanofin for RCP to LCP. Nanofin with l_x = 95 nm, l_y = 240 nm is chosen for single metalens. (d) Top-view optical microscope image and (e) top-view SEM image of the fabricated SiN_x metalens with a diameter of 250 μm. Scale bar: 50 μm. (f) Side-view SEM image of the same metalens. Scale bar: 2 μm.

Section 3: Imaging characterization of singlet-metalens PMID.

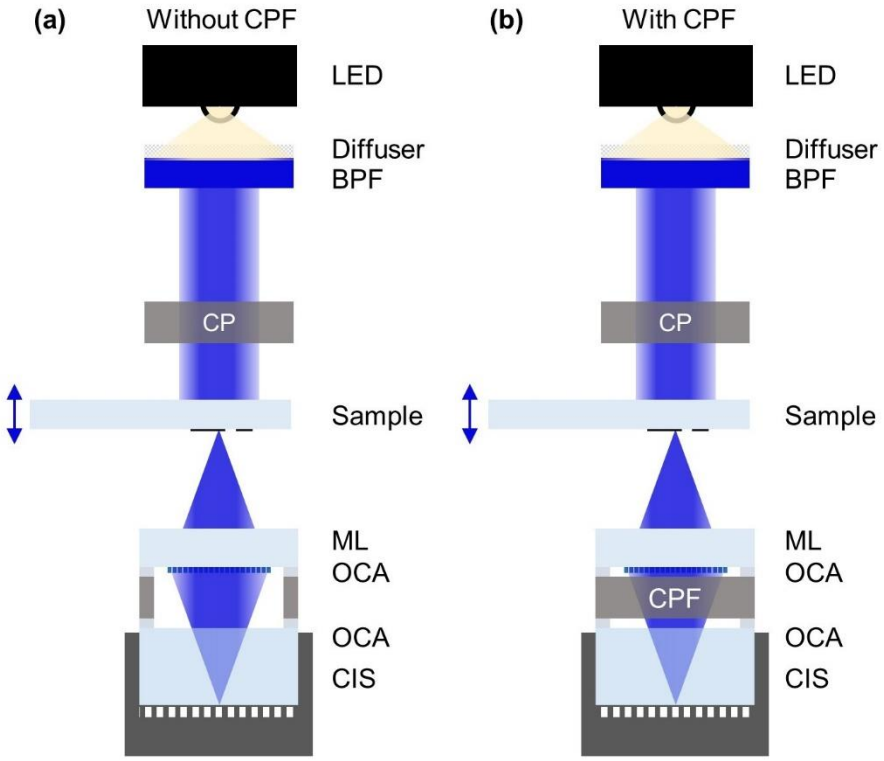

Fig. S2 The optical setups for imaging. (a) Without CPF. (b) With CPF. BPF: band-pass filter, Thorlabs, FB-10 series (410 nm-650 nm). CP: circular polarizer. CPF: circular polarization filter, thickness = 220 μm. ML: metalens. OCA: optical clear adhesive, Tesa, 69402. CIS: CMOS image sensor, DMM 27UJ003-ML, pixel size: 1.67 μm × 1.67 μm.

Wideband imaging of single metalens: We have designed three single metalenses with different magnifications. The images of 1951 USAF resolution test chart are shown in Figs. S3-S5, respectively for 1×, 2×, 3× metalenses without/with CPF. The images are captured with proper intensity to make sure the captured images not overexposed. The wavelength range of three metalenses are diverse. The smaller the magnification is, the wider the imaging bandwidth. And with the integration of CPF, the wavelength range of imaging was also enlarged. There are several

reasons that limit the imaging bandwidth. (1) The efficiency and SNR of metalens. Silicon nitride is chosen to design the metalenses. Figure S6 shows the PCR and T of the chosen nanofin over the whole visible spectrum from 400 to 700 nm. The more the wavelength deviates from the design wavelength, the smaller the PCR. (2) The efficiency of CPF. Although CPF can almost filter out unmodulated co-polarized stray light totally, when the transmittance of modulated light is very small, the SNR of image is bad. (3) Image magnification. Amplification imaging makes the average intensity weak, resulting in low SNR of magnified image. What's more, the operating wavelength is also limited by the spectrum of the illumination LED.

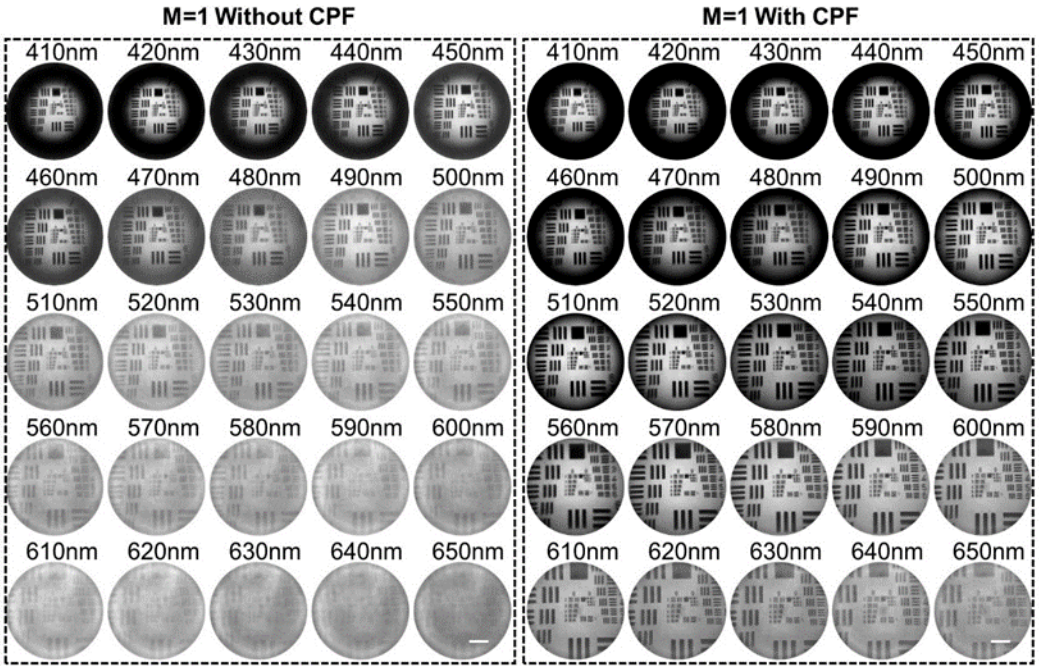

Fig. S3 The images of 1951 USAF resolution test chart with 1× metalens from 410 to 650 nm. Scale bar: 50 μm.

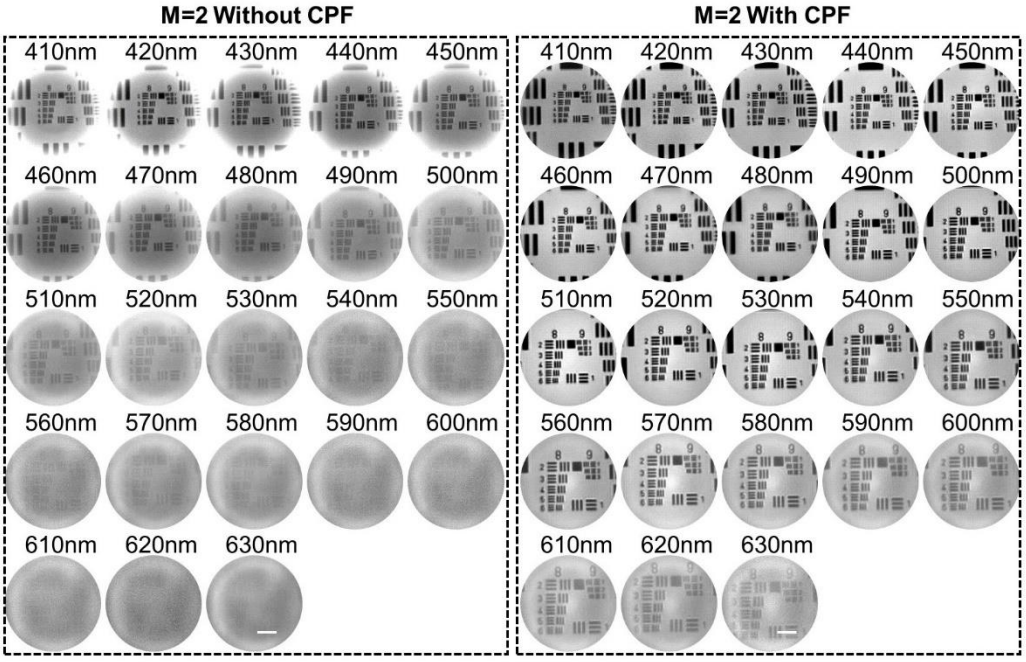

Fig. S4 The images of 1951 USAF resolution test chart with 2× metalens from 410 to 630nm. Scale bar: 50 μm.

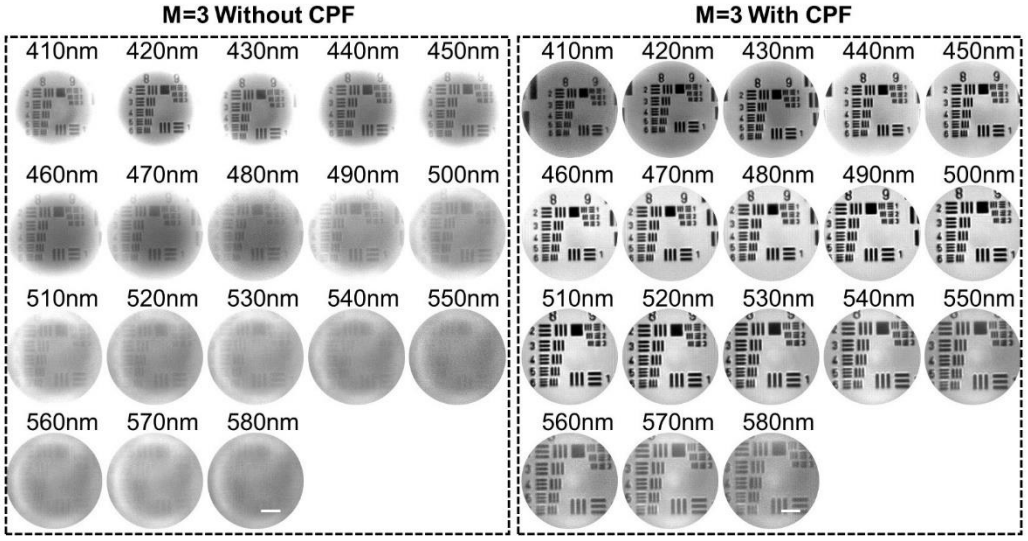

Fig. S5 The images of 1951 USAF resolution test chart with 3× metalens from 410 to 580 nm. Scale bar: 50 μm.

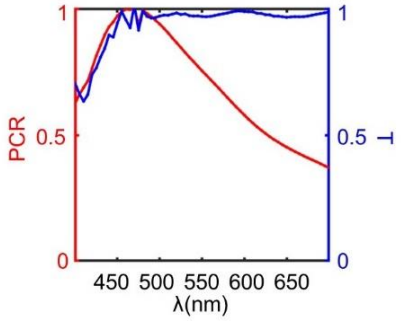

Fig. S6 The simulated polarization conversion rate (PCR) and transmittance (T) of the chosen nanofin (l_x = 95 nm, l_y = 240 nm) over the whole visible spectrum from 400 to 700 nm. The conversion rate is defined as the transmitted optical power ratio with opposite helicity to the incident circularly polarized optical power.

Detailed SNR analysis of wideband imaging: For SNR can quantitatively evaluate the quality of imaging, we systematically calculated the imaging SNR for three metalenses without/with CPF. We calculated SNR based on multiple sets of signals and noises and computed their average value as the final SNR, as shown in Fig. S7. The SNR of metalens with larger magnification has a more significant improvement.

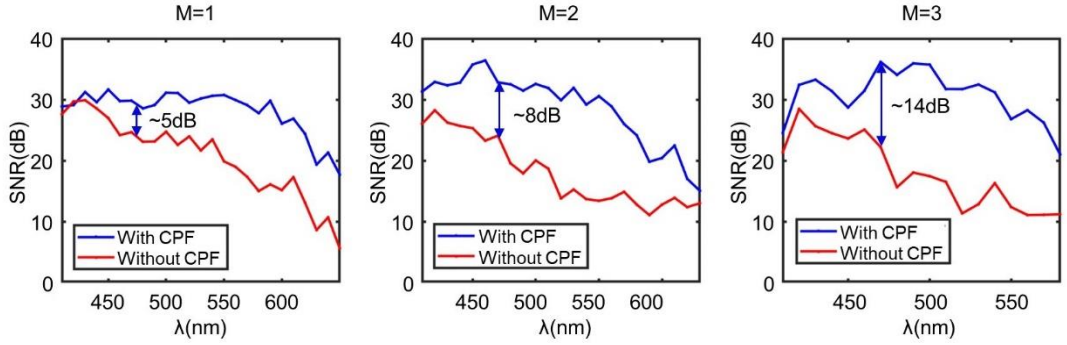

Fig. S7 The SNR of three metalenses from Figs. S3-S5.

Depth-of-field image of bio-specimen: Figure S8 shows the images of the tentacle of the mosquito male whole mount (w.m.) from 410 to 560 nm, corresponding to DOF of ~236 μm. And the images of the HUVECs in solution from 450 to 540 nm are depicted in Fig. S9.

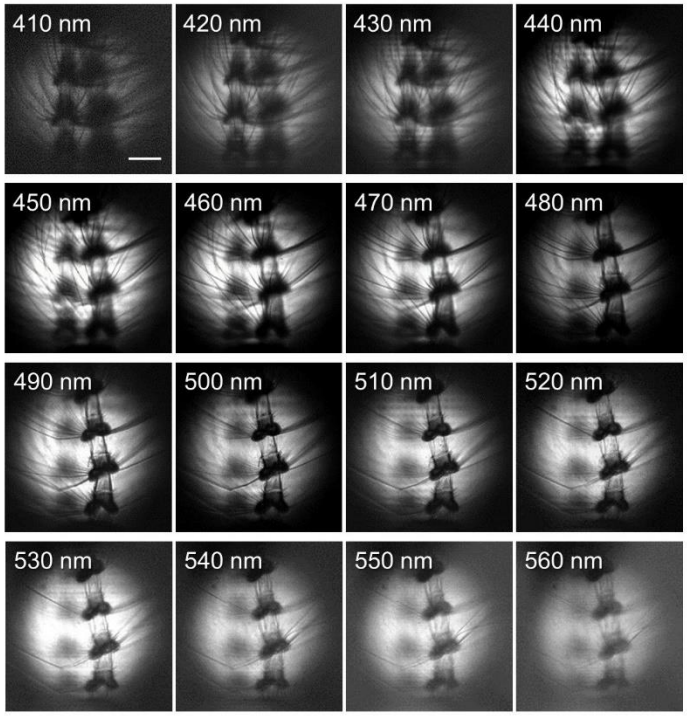

Fig. S8 The images of the tentacle of the mosquito male w.m. with 2× metalens from 410 to 560 nm (corresponding to DOF of ~236 μm). Scale bar: 50 μm.

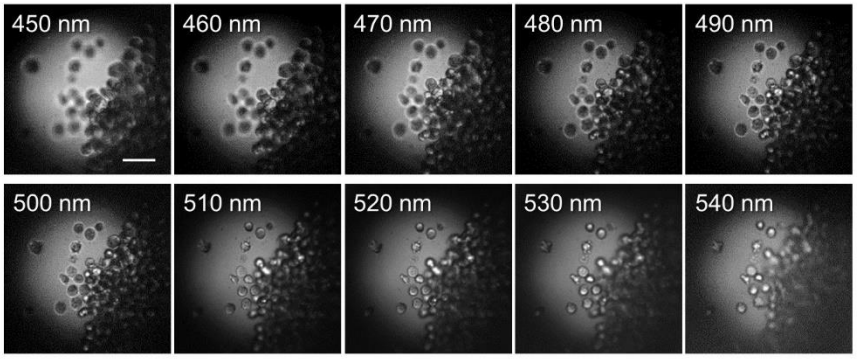

Fig. S9 The images of the HUVECs in solution with 2× metalens from 450 to 540 nm. Scale bar: 50 μm.

Section 4: Design of chip-scale metalens.

Design of chip-scale metalens: The chip-scale metalens was designed with the co-and-cross-polarization-multiplexed dual-phase approach mentioned in the manuscript. As is shown in Fig. 3(a), two sets of metalens array are utilized to make up the blind area among limited FOV of metalens. Here, the phase profiles of the metalens array are designed following aplanatic phase distribution

$$\varphi_{RCP\to RCP} = -\frac{2\pi}{\lambda}\left(\sqrt{x^2+y^2+s^2}+\sqrt{x^2+y^2+s'^2}\right), \tag{S1}$$

$$\varphi_{LCP\to RCP} = -\frac{2\pi}{\lambda}\left(\sqrt{(r-abs(x))^2+(r-abs(y))^2+s^2}+\sqrt{(r-abs(x))^2+(r-abs(y))^2+s'^2}\right), \tag{S2}$$

where λ is the design wavelength, x and y are the coordinates of each nanofin, r is the radius of metalens element, s is the object distance and s' is the image distance. The phase of incident orthogonal circularly polarized light can be independently modulated by changing the dimension and rotation of nanofin. To obtain the designed phase distribution, we chose rectangular SiN_x nanofin with a height of 1 μm as nanostructure. A parameter sweep was performed with finite-difference time-domain (FDTD) simulations at the designed wavelength. The length l_x and width l_y ranged from 60 nm to 250 nm with lattice constant of 300 nm. In this way, a library can be compiled so that structures which provide a match for imparting the desired phase shifts $\{\varphi_{RCP\to RCP},\varphi_{LCP\to RCP}\}$ can always be chosen given an appropriate figure of merit. Simulated amplitude distributions of the transmitted RCP and LCP light with nanofins' geometric parameters are shown in Fig. S10(a). Table S1 lists the detailed parameters of the selected nanofins

corresponding to the marks in Fig. S10(a).

Further, we performed 3D simulations to evaluate the performance of metalens array. For constraints of the simulation memory and time, we simulated a 2×2 metalens array including 4 LCP and 1 entire RCP lens (shown as Fig. S10(b)) with the same NA as the real chip-scale metalens but a smaller size of 6 μm. Figure S10(c) shows the results focusing at f = 9 μm for x-polarized, LCP and RCP incidence with RCP CPF respectively.

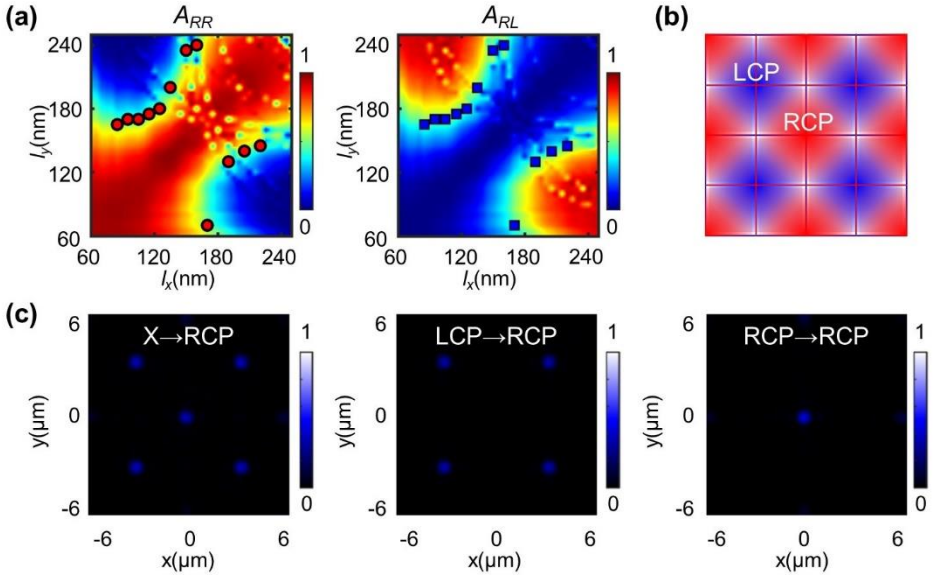

Fig. S10 Simulations for chip-scale metalens. (a) Simulated amplitude of the transmitted RCP and LCP light with the nanofins' geometric parameters under RCP incidence. (b) Schematic of chip-scale metalens for LCP (blue) and RCP (red) incidence. (c) The simulation intensity profiles of the 2×2 metalens array with CPF for x-polarized, LCP and RCP light incidence.

	l_x/nm	l_y/nm	A_{RR}	A_{RL}	$\varphi_{RR}/(\pi/6)$	$\varphi_{RL}/(\pi/6)$	T/%
1	95	170	0.4526	0.5249	0.02	9.00	97.74
2	105	170	0.4422	0.5313	0.86	9.86	97.34
3	115	175	0.4837	0.5021	1.94	10.95	98.58
4	125	180	0.5118	0.4566	3.15	0.20	96.84
5	190	130	0.4878	0.4977	4.20	7.20	98.55
6	135	200	0.5377	0.4593	5.00	1.96	99.71
7	205	140	0.5152	0.4598	5.83	8.84	97.50
8	220	145	0.4951	0.4640	7.13	10.16	95.91
9	150	235	0.4771	0.4346	8.12	5.11	91.17
10	160	240	0.4490	0.5306	9.08	6.11	97.97
11	170	70	0.4958	0.4837	10.03	1.03	97.95
12	85	165	0.5162	0.4672	10.92	7.90	98.34

Table S1. Parameters of the selected nanofins.

Section 5: Proceeding of image stitching.

By simply switching the polarization station of incident light, we can obtain two raw images from the chip-scale metalens device, as depicted in Fig. 3(c). To get the reconstructed image in Fig. 3(d), we need to stitch two sets of sub-images together. The image stitching process is shown in Fig. S11.

For the non-uniform illumination and noise response of image sensor, direct stitching brings obvious stitching marks and low SNR. These problems can be solved by background subtraction before sub-image extraction. The raw images, background images and images after background

subtraction for LCP and RCP incident light are shown in Figs. S11(a) and S11(b). The imaging quality of center region are better than that of edge region for single metalens, so mask function was used to weaken the influence of edge region that with worse imaging quality. The mask function is as follows (shown as Fig. S11(c))

$$F_{Mask}(x,y) = e^{-((x-x_c)^2+(y-y_c)^2)/(D/4)^2}, \tag{S3}$$

where x and y correspond to the position coordinates on the elemental metalens, x_c and y_c are the center coordinates of the metalens and D is the diameter of the metalens. After sub-image extraction, mask processing was performed as depicted in Fig. S11(d). Figures S11(e) and (f) show image stitching of both mask images and sub-images after mask processing. After normalization, the final stitched wide-field image can be obtained (see Fig. S11(g)), which has high SNR and good imaging quality.

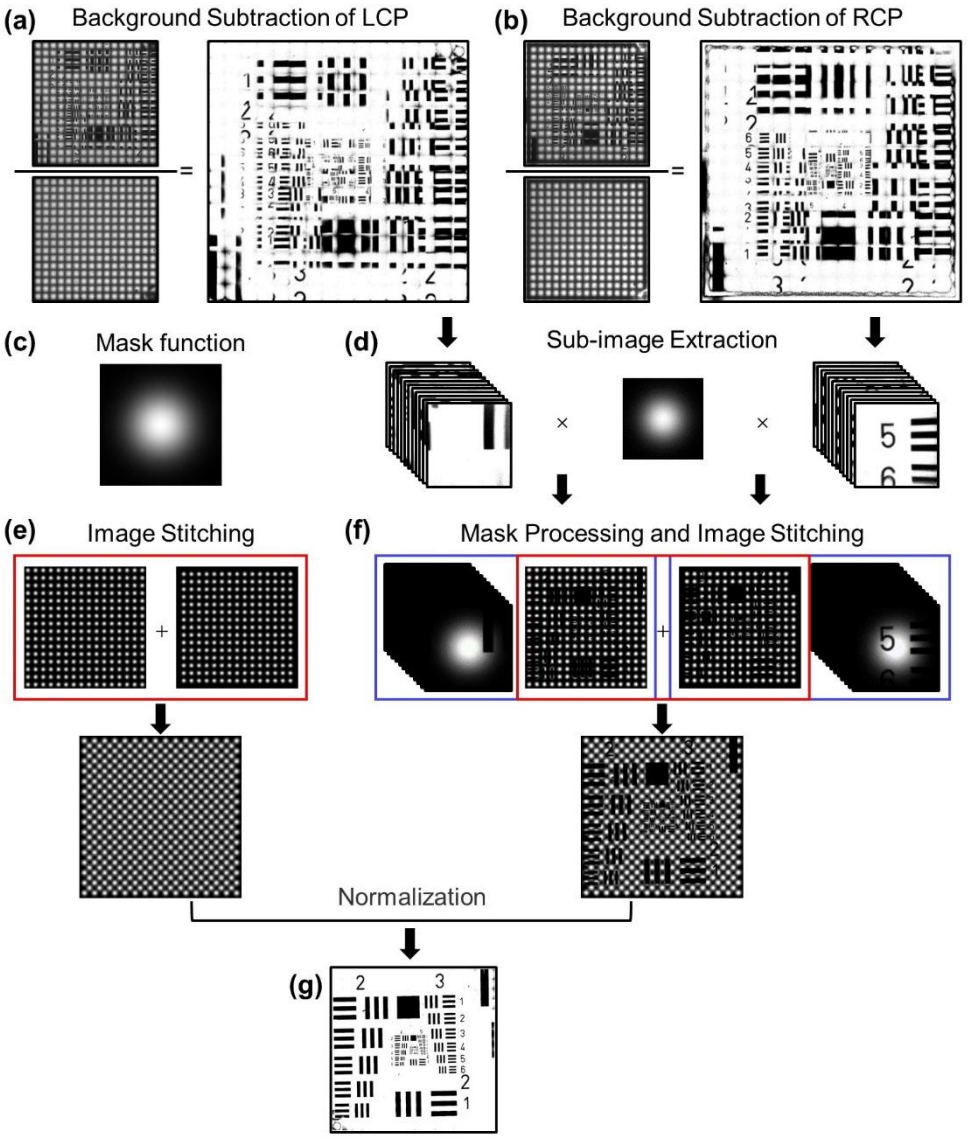

Fig. S11 Proceeding of image stitching of chip-scale metalens. (a) Raw images of USAF and background for RCP and the image after background subtraction. (b) Raw images of USAF and background for LCP and the image after background subtraction. (c) Mask function for weakening the effect of distortion. (d) Sub-images for images after background subtraction in (a) and (b). (e) Stitched image of mask function. (f) Stitched image of sub-images after mask processing. (g) Final wide-field image after normalization.

Section 6: Imaging characterization of chip-scale PMID.

Wide field-of-view imaging of bio-specimens: In addition to the bio-specimens mentioned in the main manuscript, blood smear, pine stem cross section (c.s.), tongue longitudinal section (l.s.) and mosquito male whole mount (w.m.) are imaged by the chip-scale PMID. Figure S12 shows the raw images, stitched images and zoom-in stitched images corresponding to the same region that recorded by Olympus microscope camera with 10× objective. Full FOV of the chip-scale PMID is ~7.5 times the FOV of Olympus microscope camera with 10× objective.

Note that for the traditional microscope, the objectives are achromatic for wideband wavelength to get a color image with good quality, while our PMID sacrifices the color information to obtain the DOF information. In other words, only grayscale images can be obtained. Nevertheless, in the viewpoint of image quality, our chip-scale PMID acquired single-wavelength image quality is comparable to that of a traditional microscope in despite of its broadband illumination, and our images even have a higher image contrast.

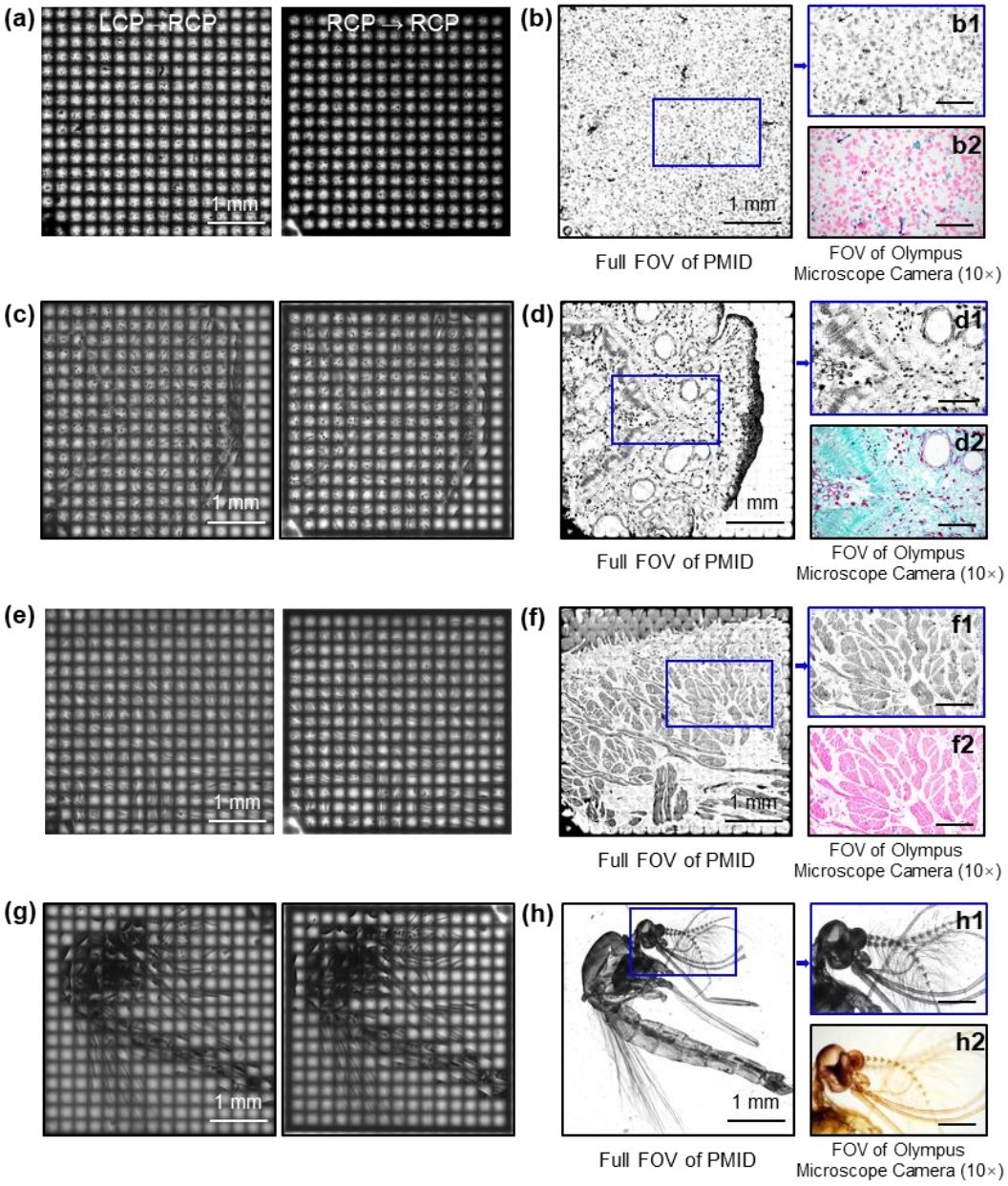

Fig. S12 Wide field-of-view images of bio-specimens. (a) Raw images of blood smear at 470 nm. (b) Stitched image from sub-images of (a). (c) Raw images of pine stem c.s. at 470 nm. (d) Stitched image from sub-images of (c). (e) Raw images of tongue l.s. at 470 nm. (f) Stitched image from sub-images of (e). (g) Raw images of mosquito male w.m. at 470 nm. (h) Stitched image from sub-images of (g). Scale bar: 400 μm.

Wideband imaging of chip-scale PMID: With CPF integration, the PMID can effectively achieve wideband imaging which is impossible for the system without CPF because the efficiency decreasing when operating wavelength shifts. After filtering out the unmodulated light, images with good quality can also be realized from 450 nm to 510 nm (see Fig. S13). With the increasing of the operating wavelength, the magnification of chip-scale PMID is larger, corresponding to better resolution. However, the magnification of the PMID is limited because of the information loss. When the operating wavelength is 510 nm, the white stitching marks of the wide-field stitched image can be found for the reason mentioned above.

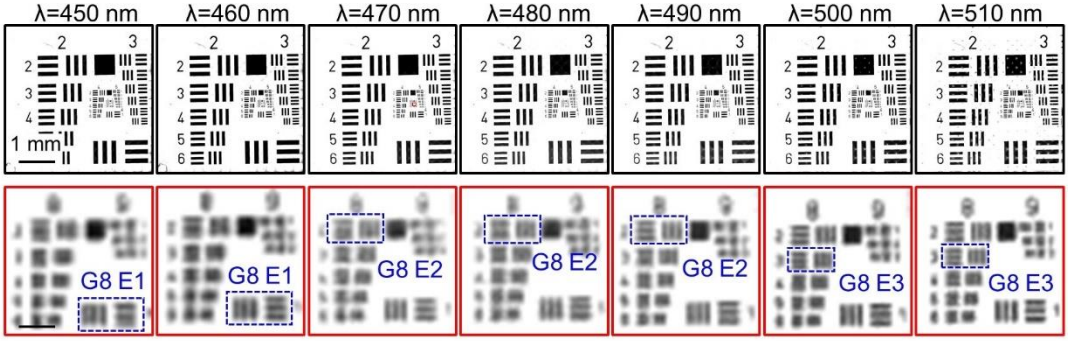

Fig. S13 Wideband imaging of USAF resolution test chart (450 nm-510 nm). Scale bar: 10 μm.

Depth of field characterization: Wideband imaging in our system, in another words, is depth-of-field imaging for the fixed image distance. So, we further calibrated depth of field with nanoslit, as depicted in Fig. S14. The experimental results show the depth of field of the PMID is ~46.6 μm at 470 nm. It can be non-negligible that the resolution is pixel-limited, which influences the accuracy of the DOF that measured.

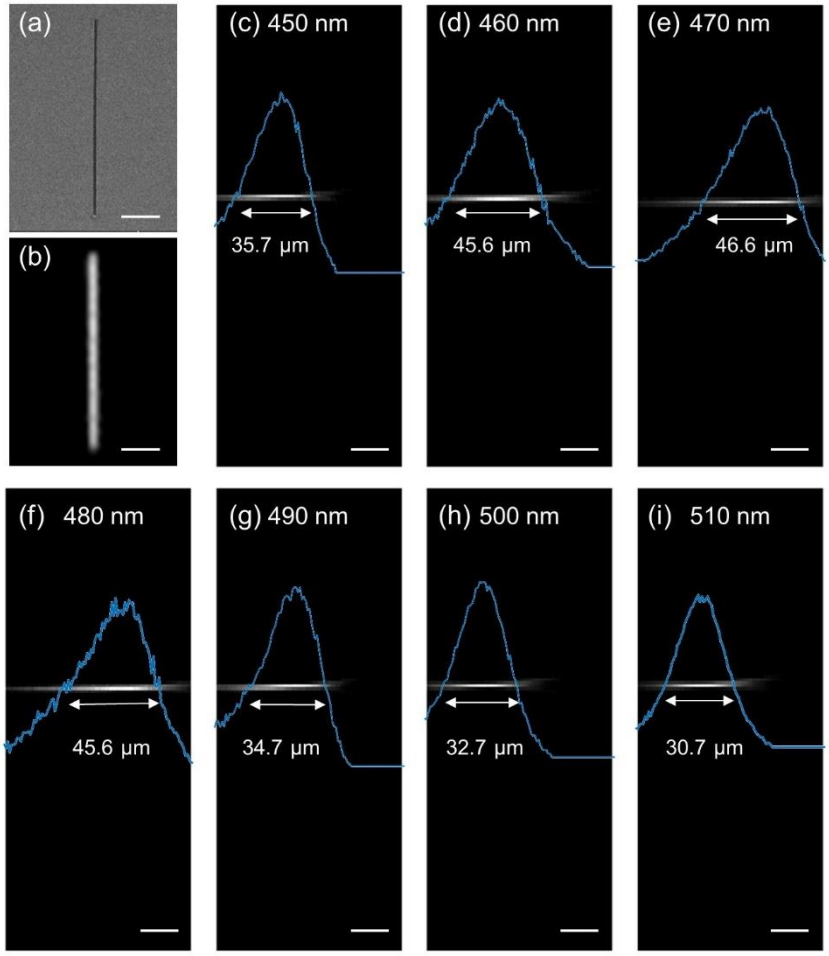

Fig. S14 Depth of field characterization of the chip-scale PMID. (a) SEM image of a nanoslit sample (50 μm × 800 nm). Scale bar: 10 μm. (b) Image of the nanoslit sample. Scale bar: 10 μm. (c-i) Longitudinal cross section of the moving slit as a 2D point source imaged with the chip-scale PMID at different wavelength (450 nm-510 nm, filter bandwidth of 10 nm). Scale bar: 20 μm.

Depth-of-field imaging of HUVECs in solution: The chip-scale PMID was used to image HUVECs in solution from 450 nm to 510 nm (see Fig. S15). Images of different operating wavelength correspond to information of different depth, so that the PMID can provide an effective liquid observation approach.

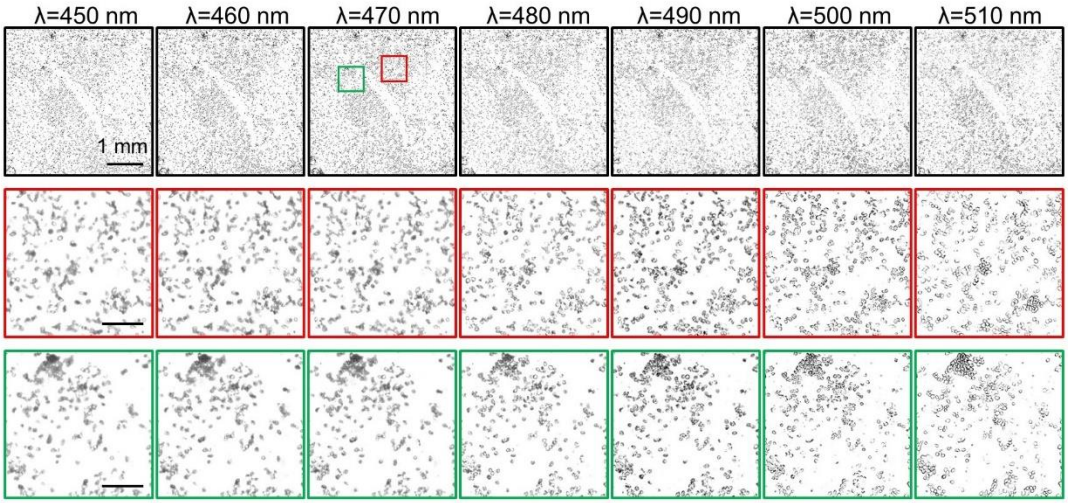

Fig. S15 Depth-of-field images of HUVECs in solution (450 nm-510 nm). Scale bar: 200 μm.

Section 7: Compact microscope protype.

For totally integration of our chip-scale PMID with the light source module, we realized a compact PMID-enabled prototype (PMS), as shown in Fig. 5(b). The size of the compact prototype is $3\times3.5\times4$ cm^3. The operation of PMS has been provided in Supplementary Video (Video 2).

The integration of light source module: The light source module includes the circuit board, LED, polarizer and LC. The polarizer is directly attached to the blue LED, used to generate circularly polarized light. Together with LC, the polarization of the incident light can be switched without any mechanical movement simply by applying an electrical bias to the LC. Two different voltage signals are applied between the ITO (Indium Tin Oxide) electrodes of the LC, which makes LC act as full-wave plate or half-wave plate corresponding to two orthogonal circularly polarized light, respectively.

Interactive control system: The use of our microscope prototype is totally controlled by an interactive control system (called Pocket Microscope System), as shown in Video 2. The system can modulate the polarization of incident light, shoot image and return stitched image. Further, we used the microscope prototype together with the control system to image bio-specimens at 470 nm (see Fig. S16).

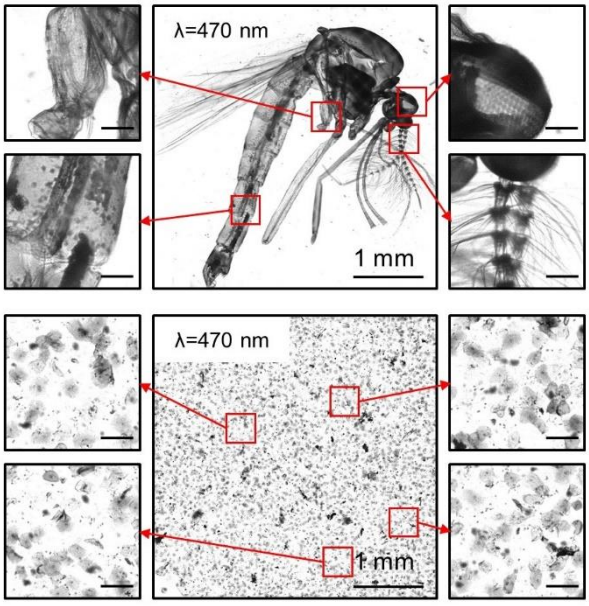

Fig. S16 Wide field-of-view images of bio-specimens (mosquito male w.m. & blood) with the microscope prototype. Scale bar: 100 μm.